

Manuscript Number:

Title: Colocalization of Outflow Segmentation and Pores Along the Inner Wall of Schlemm's Canal

Article Type: Research Article

Keywords: Schlemm's Canal; Inner Wall; Endothelium; Segmentation; Pores; Juxtacanalicular Tissue; Perfusion; Human Eyes.

Corresponding Author: Dr Darryl Ray Overby, PhD

Corresponding Author's Institution: Imperial College London

First Author: Sietse Theodoor Braakman

Order of Authors: Sietse Theodoor Braakman; A. Thomas Read, PhD; Darren W.H. Chan, PhD; C. Ross Ethier, PhD; Darryl R Overby, PhD

**Abstract:** All aqueous humor draining through the conventional outflow pathway must cross the endothelium of Schlemm's canal (SC), likely by passing through micron-sized transendothelial pores. SC pores are non-uniformly distributed along the inner wall endothelium, but it is unclear how the distribution of pores relates to the non-uniform or segmental distribution of aqueous humor outflow through the trabecular meshwork. It is hypothesized that regions in the juxtacanalicular tissue (JCT) with higher local outflow should coincide with regions of greater inner wall pore density compared to JCT regions with lower outflow. Three pairs of non-glaucomatous human donor eyes were perfused at 8 mmHg with fluorescent tracer nanospheres to decorate local patterns of outflow segmentation through the JCT. The inner wall was stained for CD31 and/or vimentin and imaged en face using confocal and scanning electron microscopy (SEM). Confocal and SEM images were spatially registered to examine the spatial relationship between inner wall pore density and tracer intensity in the underlying JCT. For each eye, tracer intensity, pore density (n) and pore diameter (D) (for both transcellular "I" and paracellular "B" pores) were measured in 4-7 regions of interest (ROIs; 50 x 150  $\mu$ m each). Analysis of covariance was used to examine the relationship between tracer intensity and pore density, as well as the relationship between tracer intensity and three pore metrics (nD, nD2 and nD3) that represent the local hydraulic conductivity of the outflow pathway as predicted by various hydrodynamic models. Tracer intensity in the JCT correlated positively with local pore density when considering total pores ( $p = 0.044$ ) and paracellular B pores on their own ( $p = 0.016$ ), but not transcellular I-pores on their own ( $p = 0.54$ ). Local hydraulic conductivity as predicted by the three hydrodynamic models all showed a significant positive correlation with tracer intensity when considering total pores and B-pores ( $p < 0.0015$  and  $p < 10^{-4}$ ) but not I-pores ( $p > 0.38$ ). These data suggest that aqueous humor passes through micron-sized pores in the inner wall endothelium of SC. Paracellular B-pores appear to have a dominant contribution towards transendothelial filtration across the inner wall relative to transcellular I-pores. Impaired pore formation, as previously described in glaucomatous SC cells, may thereby contribute to greater outflow heterogeneity, outflow obstruction, and IOP elevation in glaucoma.

Suggested Reviewers: Jeffrey Ruberti PhD

Associate Professor, Bioengineering, Northeastern University, Boston, MA, USA

j.ruberti@neu.edu

Mark C Johnson PhD

Professor, Biomedical Engineering, Northwestern University, Evanston, IL, USA

m-johnson2@northwestern.edu

Christopher L Passaglia PhD

Associate Professor, Biomedical Engineering, Boston University School of Medicine, Boston, MA, USA

psagls@bu.edu

Thomas Freddo PhD

Professor, Optometry and Vision Science, University of Waterloo, Waterloo, ON, Canada

tfreddo@uwaterloo.ca

Arthur J Sit MD

Associate Professor, Ophthalmology, Mayo Clinic, Rochester, MN, USA

sit.arthur@mayo.edu

September 19, 2014

Editorial Office  
*Experimental Eye Research*

Dear Editors:

Please find attached our manuscript titled "Colocalization of Outflow Segmentation and Pores Along the Inner Wall of Schlemm's Canal", which we hereby submit for consideration for publication in *Experimental Eye Research*.

Our paper examines the hypothesis that regions of increased aqueous humour outflow through the juxtacanalicular tissue coincide with regions of increased pore density in Schlemm's canal (SC) endothelium. Our research confirms that pores serve as pathways for aqueous humour filtration across SC inner wall. This is important because SC pore density is reduced in glaucoma, and reduced pore density may contribute to the outflow obstruction and ocular hypertension characteristic of the disease.

Thank you for considering our manuscript, and we look forward to your kind reply.

Sietse Braakman and Darryl Overby

Highlights:

- Enucleated human eyes were perfused with fluorescent tracer nanospheres to visualize the patterns of outflow through the juxtacanalicular tissue (JCT).
- Correlative microscopy was used to spatially register fluorescent images of tracer intensity in the JCT with scanning electron micrographs of micron-sized pores along the inner wall endothelium of Schlemm's canal (SC).
- Regions of greater tracer intensity coincided with regions of greater pore density, suggesting that aqueous humor passes through pores in the inner wall endothelium of SC.
- Paracellular "B" pores appeared to have a dominant contribution towards transendothelial filtration across the inner wall relative to transcellular "I" pores.
- Impaired pore formation, as previously described in glaucomatous SC cells, may thereby contribute to greater outflow heterogeneity, outflow obstruction, and IOP elevation in glaucoma.



# Colocalization of Outflow Segmentation and Pores Along the Inner Wall of Schlemm's Canal

Sietse T. Braakman<sup>1</sup>, A. Thomas Read<sup>2</sup>, Darren W.-H. Chan<sup>2</sup>, C. Ross Ethier<sup>1,3</sup>,  
Darryl R. Overby<sup>1</sup>

<sup>1</sup>Department of Bioengineering, Imperial College London, London, United Kingdom

<sup>2</sup>Department of Ophthalmology and Vision Sciences, University of Toronto, Canada

<sup>3</sup>Coulter Department of Biomedical Engineering, Georgia Institute of Technology and Emory University, USA

Support: A grant from National Glaucoma Research, (G2009-032) a Program of The BrightFocus Foundation (Formerly the American Health Assistance Foundation), and the National Eye Institute (EY019696).

Total word count: 7075, excluding abstract, including figure and table captions

Abstract word count: 369

Corresponding author: Dr. Darryl R. Overby  
Department of Bioengineering  
Imperial College London  
London SW7 2AZ  
United Kingdom  
+44 (0) 20 7594 6376  
d.overby@imperial.ac.uk

# 1 Abstract

2 All aqueous humor draining through the conventional outflow pathway must  
3 cross the endothelium of Schlemm's canal (SC), likely by passing through micron-  
4 sized transendothelial pores. SC pores are non-uniformly distributed along the inner  
5 wall endothelium, but it is unclear how the distribution of pores relates to the non-  
6 uniform or *segmental* distribution of aqueous humor outflow through the trabecular  
7 meshwork. It is hypothesized that regions in the juxtacanalicular tissue (JCT) with  
8 higher local outflow should coincide with regions of greater inner wall pore density  
9 compared to JCT regions with lower outflow.

10 Three pairs of non-glaucomatous human donor eyes were perfused at 8 mmHg  
11 with fluorescent tracer nanospheres to decorate local patterns of outflow  
12 segmentation through the JCT. The inner wall was stained for CD31 and/or vimentin  
13 and imaged *en face* using confocal and scanning electron microscopy (SEM).  
14 Confocal and SEM images were spatially registered to examine the spatial  
15 relationship between inner wall pore density and tracer intensity in the underlying  
16 JCT. For each eye, tracer intensity, pore density ( $n$ ) and pore diameter ( $D$ ) (for both  
17 transcellular "I" and paracellular "B" pores) were measured in 4-7 regions of interest  
18 (ROIs; 50 x 150  $\mu\text{m}$  each). Analysis of covariance was used to examine the  
19 relationship between tracer intensity and pore density, as well as the relationship  
20 between tracer intensity and three pore metrics ( $nD$ ,  $nD^2$  and  $nD^3$ ) that represent the  
21 local hydraulic conductivity of the outflow pathway as predicted by various  
22 hydrodynamic models.

23 Tracer intensity in the JCT correlated positively with local pore density when  
24 considering total pores ( $p = 0.044$ ) and paracellular B pores on their own ( $p = 0.016$ ),  
25 but not transcellular I-pores on their own ( $p = 0.54$ ). Local hydraulic conductivity as

1 predicted by the three hydrodynamic models all showed a significant positive  
2 correlation with tracer intensity when considering total pores and B-pores ( $p <$   
3  $0.0015$  and  $p < 10^{-4}$ ) but not I-pores ( $p > 0.38$ ).

4       These data suggest that aqueous humor passes through micron-sized pores in  
5 the inner wall endothelium of SC. Paracellular B-pores appear to have a dominant  
6 contribution towards transendothelial filtration across the inner wall relative to  
7 transcellular I-pores. Impaired pore formation, as previously described in  
8 glaucomatous SC cells, may thereby contribute to greater outflow heterogeneity,  
9 outflow obstruction, and IOP elevation in glaucoma.

# 1 Introduction

2       The conventional outflow pathway is the predominant route of aqueous humor  
3 outflow, and the increase in intraocular pressure (IOP) associated with many cases  
4 of primary open angle glaucoma (POAG) is due to increased conventional outflow  
5 resistance (Grant, 1963). Within the conventional outflow pathway, the majority of  
6 outflow resistance appears to be generated in the vicinity of the inner wall  
7 endothelium of Schlemm’s canal (SC) and the juxtacanalicular tissue (JCT) (Lütjen-  
8 Drecol, 1973; Mäepea and Bill, 1992), but the hydrodynamic details of how aqueous  
9 humor flows through these tissues remain unclear.

10       All conventional aqueous outflow must somehow filter across the inner wall  
11 endothelium of SC, presumably by passing through micron-sized pores in an  
12 otherwise continuous endothelium containing tight junctions (M. C. Johnson, 2006).  
13 In glaucoma, inner wall pore density is reduced by up to five-fold compared to  
14 normal eyes (Allingham et al., 1992; M. C. Johnson et al., 2002), suggesting that  
15 impaired pore formation may contribute to outflow obstruction and IOP elevation  
16 characteristic of glaucoma. Two types of pores exist: transcellular “I” pores that pass  
17 through individual SC cells, and paracellular “B” pores that pass through the junction  
18 between neighboring SC cells (Ethier et al., 1998). However, the contribution of each  
19 pore type to filtration across the inner wall and whether one pore type has a  
20 dominant role remain unknown.

21       Drainage through the conventional outflow pathway is non-uniform or  
22 *segmental* around the circumference of the trabecular meshwork (TM) (de Kater et  
23 al., 1989), over both a “macro” scale (order of mm) and over a “micro” scale (order of  
24 a few  $\mu\text{m}$ ; Figure 1) (Chang et al., 2014; Lu et al., 2008). Furthermore, inner wall  
25 pores are non-uniformly distributed along the inner wall endothelium (Allingham et

1 al., 1992). This study investigated the hypothesis that regions of higher local outflow  
2 co-localize with regions of higher local pore density along the inner wall of SC  
3 (Figure 2). To test this hypothesis, fluorescent tracer nanospheres were perfused  
4 into post mortem human eyes, SC was micro-dissected to visualize the inner wall *en*  
5 *face*, and correlative light and electron microscopy was used to image the  
6 distribution of tracer and location of pores along the inner wall. A spatial correlation  
7 was observed between local tracer intensity and local pore density, suggesting that  
8 at least some pores are fluid-conducting structures that respond to local mechanical  
9 stimuli induced by flow and/or pressure drop across the inner wall.

## 1 Methods

### 2 Reagents

3 Dulbecco's phosphate buffered saline (DPBS), glucose, gelatin, Triton X-100,  
4 tannic acid, guanidine hydrochloride and goat serum were acquired from Sigma  
5 Aldrich (Austin, TX, USA). Glutaraldehyde, formaldehyde, ethanol, osmium tetroxide  
6 and hexamethyldisilazane were purchased from EMS Diasum (Hatfield, PA, USA).  
7 Fluorescent tracer nanospheres (20 nm, sulfate-coated; F8845), Alexa647 goat anti-  
8 mouse IgG, Alexa 546 goat anti-rabbit and DAPI were obtained from Life  
9 Technologies (Austin, TX, USA). Mounting medium and mouse anti-human CD31  
10 antibody (clone JC70A) were obtained from DAKO (Glostrup, Denmark). Rabbit anti-  
11 human vimentin antibodies (clone EPR3776) were obtained from Abcam  
12 (Cambridge, MA, USA).

13

### 14 Whole Eye Perfusion

15 Three pairs of ostensibly normal human eyes were obtained from donors aged  
16 67, 78 and 80 through the Eye Bank of Canada (Ontario Division, Toronto, Canada),  
17 Table 1. The temperature of the eye was maintained by submersion in a bath of  
18 DPBS at 34°C. A needle was inserted through the corn ea with the tip positioned in  
19 the posterior chamber, and the eye was perfused at a constant pressure of 8 mmHg  
20 following established methods (Ethier et al., 1998; 1993). The perfusion fluid was  
21 DPBS containing CaCl<sub>2</sub>, MgCl<sub>2</sub> and 5.5 mM glucose that was filtered through a 0.22  
22 µm syringe filter prior to use (referred to as 'DBG'). After perfusion with DBG for 45 –  
23 90 minutes to measure baseline outflow facility (Table 1), the anterior chamber was  
24 exchanged with DBG containing 0.005% w/v fluorescent tracer nanospheres. After  
25 the exchange, the eye was perfused for 30 minutes with tracer to label the patterns

1 of outflow through the TM, while recording 'tracer' facility (Table 1). The anterior  
2 chamber was then exchanged with either DBG alone or DBG containing 2% gelatin,  
3 and the eye was perfused until it reached a steady 'post-tracer' facility (Table 1)  
4 typically within 30 – 40 minutes. Gelatin was used to preserve the distribution of  
5 tracer within the tissue, following Johnson et al. (M. C. Johnson et al., 1990), but  
6 gelatin did not appear to affect outflow facility when compared to the paired control  
7 eye. The perfusion was terminated by clamping the perfusion tubing and then  
8 immediately placing the eyes on wet ice for 15 – 20 minutes. The perfusion needles  
9 were kept in place during the cooling period, but with the tubing clamped, the  
10 pressure in the eye decreased slowly over several minutes on account of drainage  
11 through the conventional outflow pathway. Following the cooling period, the globes  
12 were cut open near the equator and immersion fixed in ice cold 3% formaldehyde in  
13 DBG.

14

## 15 **Dissection**

16 The eyes were hemisected, the vitreous humor and lens were removed and the  
17 anterior segment was cut into quadrants. Each quadrant was cut into wedges for  
18 microdissection to expose approximately 2-3 mm along the circumference of the  
19 inner wall *en face*, as previously described (Ethier et al., 2004). Briefly, the tissue  
20 wedges containing the inner wall, JCT and TM, were separated from the ciliary body  
21 and iris root. SC was incised along its posterior margin and opened such that the TM  
22 and adherent inner wall of SC could be reflected anteriorly. The inner wall and  
23 underlying TM were fluorescently stained for the endothelial marker CD31, the  
24 intermediate filament vimentin, and the nuclear stain DAPI. Specifically, the tissue  
25 was permeabilized at room temperature (RT) for 5 minutes with 0.2% Triton X-100 in

1 DPBS and blocked at RT for 30 minutes with 10% goat serum. Tissue was then  
2 labeled with mouse anti-human CD31 IgG (dilution 1:30) and rabbit anti-human  
3 Vimentin IgG (1:200) overnight at 4°C. After three 5 minute washes with DPBS, the  
4 tissue was incubated with Alexa 647 goat anti-mouse IgG (1:150) and Alexa 546  
5 goat anti-rabbit IgG (1:150) overnight at 4°C. Negative controls were prepared as  
6 above, omitting the primary antibodies. Finally, nuclei were labeled by incubating the  
7 tissue for 5 min at RT in 2 µg/mL DAPI in DPBS.

8

## 9 **Imaging**

10 One tissue wedge was imaged per eye using first confocal microscopy (to  
11 visualize tracer, CD31, vimentin and DAPI) and then scanning electron microscopy  
12 (SEM; to visualize pores). For confocal imaging, each wedge was mounted in  
13 fluorescent mounting medium and oriented such that the inner wall of SC faced  
14 upwards, overlying the adjacent JCT/TM. The tracer (Ex: 505nm/Em: 515nm), CD31  
15 (650/665), vimentin (556/573) and DAPI (358/461) were imaged *en face* using a  
16 Zeiss LSM 510 meta confocal microscope with a 25x/0.8NA objective. Images were  
17 obtained as a z-stack starting several microns above the inner wall and stretching 50  
18 – 80 µm deep into the TM. Each confocal image was corrected for uneven  
19 illumination by dividing local intensities by those from the corresponding location of a  
20 reference image taken from a well-mixed solution of fluorescent tracer. The entire  
21 surface of the inner wall (as indicated by CD31) was imaged, such that the z-stacks  
22 could be tiled together to create a complete montage for each wedge using a plug-in  
23 executed in FIJI (NIH, MD, USA) and developed by Preibisch et al. (Preibisch et al.,  
24 2009). Montages of CD31 and vimentin were created using tiles based on the  
25 maximum intensity projection through each stack. However, the tracer stacks were



1 processed to create tiles that showed tracer in only the JCT lying within 10  $\mu\text{m}$  of the  
2 inner wall. To do this, the z-position of the inner wall was defined for each pixel  
3 using a surface spline that was fit through the z-position of the maximum CD31  
4 intensity for each x,y pixel location. The tracer pixel intensity values were then  
5 averaged across the voxels lying within 10  $\mu\text{m}$  below the inner wall for each pixel  
6 location, and this value was defined as the JCT tracer intensity for the corresponding  
7 pixel. Note that this approach eliminates the influence of tracer that lies outside of  
8 the JCT while allowing the z-position of the inner wall to change across the montage,  
9 thus accounting for inner wall undulations.

10 After the confocal montage was complete, the tissue was unmounted and  
11 prepared for SEM to visualize pores along the inner wall. The tissue was rinsed in  
12 DPBS overnight at 4°C to remove the mounting media and then post-fixed in  
13 universal fixative (2.5% (v/v) glutaraldehyde and 2% (w/v) formaldehyde in  
14 Sørensen's Buffer) overnight at 4°C. The tissue was then incubated in 2% (w/v)  
15 tannic acid, 2% (w/v) guanidine hydrochloride in DPBS for two hours, followed by  
16 one hour in 1% (w/v) osmium tetroxide in DPBS. Between each solution change, the  
17 tissue was rinsed thoroughly in DPBS. The tissue specimen was then dehydrated  
18 through a graded ethanol series, followed by two changes in hexamethyldisilazane,  
19 air-dried, mounted on stubs with carbon cement, and sputter-coated with gold. An  
20 overview montage, composed of several contiguous smaller image tiles, was  
21 acquired to show the entire inner wall surface within the wedge at 300x magnification  
22 by SEM (Hitachi S-3400N VP). The overview montage was used to identify regions  
23 of damaged inner wall, to guide the selection of regions for analysis, and to perform  
24 the image registration between the confocal and SEM montages (described below).  
25 Pore counting was not performed using the overview montage but rather using SEM

1 micrographs that were re-imaged at higher magnification (10,000x; see below).

2

### 3 **Image Registration**

4       In order to investigate the spatial relationship between tracer and pores, it was  
5 necessary to spatially register the confocal and SEM montages such that the same  
6 physical point along the inner wall appeared at the same location in both images.  
7 However, tissue shrinkage during processing and differences in tissue orientation  
8 between imaging sessions led to image distortion that prevented a simple overlay of  
9 the confocal and SEM micrographs. This distortion was corrected by mapping each  
10 confocal montage onto the corresponding SEM montage using an image registration  
11 algorithm. Briefly, the image registration algorithm used common landmarks that  
12 were manually identified in the confocal and SEM montages to establish a  
13 transformation function that, when applied to the confocal montage, deformed the  
14 confocal montage in such a way that the common landmarks overlapped with those  
15 in the SEM montage. To do this, between 48 and 80 reference points were selected  
16 in the CD31 montage (for eyes 649C and 650D) or in the vimentin montage (for eyes  
17 669B, 670B, 681B and 682D) and manually matched to corresponding reference  
18 points on the SEM montage. The coordinate positions of the pixels at each reference  
19 point were used to calculate the mathematical mapping transformation using the  
20 'cp2tform' function in MATLAB (v2014a, Mathworks, Natick, MA, USA) with a linear  
21 weighted mean optimization (Goshtasby, 1988). The same mapping transformation  
22 was then applied to the tracer montage so as to spatially register the tracer and SEM  
23 montages (Figure 3).

24

### 25 **Colocalization Analysis**

1           This study compared the fluorescent tracer intensity and pore density  
2 measured within individual regions of interest (ROIs) along the inner wall of SC.  
3 Typically, 4 – 7 ROIs were examined per tissue wedge, with 31 ROIs in total, and  
4 data from each ROI yielded a single data-point for the colocalization analysis  
5 between tracer intensity and pore density. The ROI area ( $7,500 \mu\text{m}^2$ ) was chosen to  
6 contain a sufficient number of pores (~ 62 pores, assuming a pore density of 835  
7 pores/ $\text{mm}^2$  (M. C. Johnson et al., 2002)) to allow a robust sampling of the local pore  
8 density. The ROI aspect ratio ( $50 \mu\text{m} \times 150 \mu\text{m}$ ) was chosen to approximate the  
9 aspect ratio of the inner wall as viewed *en face*, with the long edge of the ROI  
10 oriented parallel to the long axis of the inner wall. Each ROI was defined within the  
11 SEM and transformed confocal montages, and the location of each ROI was chosen  
12 based on the presence of continuous CD31 staining, representing a continuous  
13 region of the inner wall that was free of cracks, debris or other damage as seen in  
14 the SEM montage. To maximize the range and provide sufficient leverage for the  
15 colocalization analysis, ROIs were typically chosen from regions with very high or  
16 very low tracer intensity, with some ROIs covering regions of moderate tracer  
17 intensity. Within each ROI the tracer intensity ( $T$ ) was measured as the average  
18 pixel intensity over the ROI area in the transformed tracer montage. Note that the  
19 pixel intensities in the tracer montage represent the depth-wise averaged pixel  
20 intensity of the tracer channel in the JCT region within  $10 \mu\text{m}$  of the inner wall (see  
21 above).

22           After ROIs were defined, each ROI was then re-imaged by SEM for pore  
23 counting. First, an image at 1500x magnification was acquired to identify any  
24 potential pore-like object, and all pore-like objects were then re-imaged at 10,000x  
25 magnification. Each 10,000x image was assigned a random identification number to

1 mask any relationship with the ROI, and the masked images were distributed to at  
2 least three observers who independently assessed each pore-like object to  
3 distinguish true pores from artifacts and to identify pore type (I or B). Pore-like  
4 objects were identified as pores if they had a smooth, flat, approximately elliptical  
5 boundary and a dark interior. Pores that fell on the border of the ROI were included  
6 only if they fell on the left or upper border. Any discrepancies in pore identification  
7 were discussed during a panel meeting until a consensus was reached, and only  
8 after all pore decisions were finalized was the image key broken. The number of  
9 pores and pore density ( $n$ , equal to the number of pores divided by the ROI area)  
10 was then calculated for each ROI, and pore diameter ( $D$ ) was computed from the  
11 measured pore area  $A$  as:  $D = \sqrt{\frac{4A}{\pi}}$ . Several higher order moments of the pore  
12 diameter ( $nD$ ,  $nD^2$ ,  $nD^3$ ) were also calculated, motivated by hydrodynamic models of  
13 flow through pores, as described below.

14

### 15 **Hydrodynamic models of inner wall hydraulic conductivity**

16 In addition to pore density, the pore diameter may also influence the local  
17 accumulation of tracer along the inner wall. Under the assumption that the tracer  
18 distribution represents the distribution of aqueous humor filtration across the inner  
19 wall, the local tracer intensity should be proportional to the local hydraulic  
20 conductivity ( $L_p^1$ ) of the outflow pathway that includes the JCT and the inner wall  
21 endothelium. Because this study did not directly assess the hydraulic properties of  
22 the JCT, the hydraulic conductivity of the JCT was assumed to be uniform. Several  
23 models to describe  $L_p$  of the inner wall with or without the JCT have been proposed

---

<sup>1</sup> The hydraulic conductivity ( $L_p$ ) is defined as the ratio of the flow rate ( $Q$ ) to the pressure drop ( $\Delta P$ ) across a hydraulically resistive barrier, normalized by the area ( $A$ ) of the barrier. Hence,  $L_p = Q/(\Delta P A)$ .

1 including the funneling model (M. C. Johnson et al., 1992) and Sampson's law (Bill  
2 and Svedbergh, 1972; Ethier et al., 1998; Grant, 1963). Each of these models  
3 expresses  $L_p$  in terms of the product of pore density ( $n$ ) and a moment of pore  
4 diameter. Specifically, for Sampson's law,  $L_p \sim nD^3$  (Happel and Brenner, 1983;  
5 Lütjen-Drecoll, 1973; Mäepea and Bill, 1992), and for the funneling model,  $L_p \sim nD$   
6 (Ethier and Coloma, 1999; Ethier et al., 2006; M. C. Johnson, 2006). Additionally, a  
7 model was considered where the hydraulic conductivity was proportional simply to  
8 inner wall porosity (total pore area/analyzed area), and hence  $L_p \sim nD^2$ . The  
9 relationship between  $TI$  and each of  $n$ ,  $nD$ ,  $nD^2$  and  $nD^3$  (which we refer to as *pore*  
10 *metrics*) was examined for total pores, I-pores and B-pores.

11

## 12 **Statistical Analysis**

13 To test whether there was a relationship between  $TI$  and any given pore metric,  
14 two separate methods were used. First, an analysis of covariance (ANCOVA) was  
15 applied to the raw data. Essentially, ANCOVA performs a linear regression on a  
16 particular pore metric as a function of  $TI$ , with each ROI contributing a single data  
17 point to the regression analysis. The linear regression was performed separately for  
18 each wedge (4-7 ROIs per wedge), but ANCOVA forces the slope of the linear  
19 regression to be the same for all wedges. ANCOVA therefore provides an estimate  
20 of the optimal slope that best describes the relationship between the pore metric and  
21  $TI$  across all wedges, and the confidence intervals on this slope are used to  
22 determine statistical significance compared to the null hypothesis of zero slope.  
23 However, because ANCOVA operates on raw data and because the raw  $TI$  and pore  
24 metrics may vary considerably between wedges of different eyes, wedges that have  
25 particularly large data values may have a disproportionate leverage on the estimated

1 slope.

2 To account for any potential bias that may occur when analyzing raw data with  
3 ANCOVA, a second method of analysis was applied using normalized data.  
4 Importantly, data normalization (described below) eliminates the variation between  
5 wedges, while preserving the variation within each wedge, such that all of the ROI  
6 data points span a similar numerical range and can be fit by a single linear  
7 regression. Because  $TI$  was normally distributed between ROIs within each wedge ( $p$   
8  $> 0.12$ , Shapiro-Wilk test),  $TI$  was normalized (or, more accurately, *studentized*)  
9 according to  $TI_{i,j}^* = \frac{TI_{i,j} - \hat{\mu}(TI_j)}{\hat{\sigma}(TI_j)}$ , where asterisks represent normalized values, the  
10 subscript  $i$  and  $j$  refer to the  $i^{th}$  ROI of the  $j^{th}$  eye, and  $\hat{\mu}$  and  $\hat{\sigma}$  represent the  
11 estimated population mean and standard deviation of  $TI$  values over all  $i$  ROIs within  
12 the  $j^{th}$  eye. Note that the normalization of  $TI$  expresses  $TI^*$  in terms of units of  
13 standard deviation from the mean for each corresponding wedge. Because the pore  
14 density and diameter have been shown to be skewed distributions (Allingham et al.,  
15 1992; Braakman et al., 2014; M. C. Johnson et al., 2002), pore metrics ( $n$ ,  $nD$ ,  $nD^2$ ,  
16  $nD^3$ ) were normalized by dividing the raw value by the mean value, where the mean  
17 for each pore metric was calculated by averaging the pore metric itself over the ROIs  
18 of the corresponding wedge. Normalized pore metrics ( $n^*$ ,  $nD^*$ ,  $nD^{2*}$ ,  $nD^{3*}$ ) were  
19 plotted as a function of  $TI^*$  including data from all wedges, and the relationship  
20 between each pore metric versus  $TI^*$  was analyzed by a single linear regression. A  
21 two-tailed Student's t-test was used to determine whether the slope of the linear  
22 regression was significantly different from zero, with significance defined at  $p < 0.05$ .  
23 All statistical analyses was performed using MATLAB (v2014a, MathWorks, MA,  
24 USA).

1           The statistical power of a regression analysis represents the probability of  
2 finding a statistically significant correlation assuming that one exists. Because only a  
3 limited number of ROIs (typically 4-7) can be physically placed within each wedge,  
4 the statistical power of a regression analysis applied to a single wedge is relatively  
5 low (~25% assuming that  $R^2 = 0.5$  and  $\alpha = 0.05$ ). To overcome this limitation, we  
6 acquired data from 31 ROIs from 6 different wedges from separate eyes, and  
7 performed the analysis on the aggregated data. This approach increased the  
8 statistical power to approximately 71% for the ANCOVA approach and 73% for the  
9 single linear regression on the normalized data (Cohen et al., 2013; Ethier et al.,  
10 1998).  
11

# 1 Results

## 2 Image Registration

3 The transformed vimentin and CD31 images co-registered well with the SEM  
4 images (Figure 4). The distance between corresponding features was typically less  
5 than 5  $\mu\text{m}$ , and the vimentin staining around nuclei and GVs corresponded very well  
6 with the same structures seen by SEM. The accuracy of the registration algorithm  
7 was therefore judged to be within a few  $\mu\text{m}$  and thus considered to be sufficient for a  
8 colocalization analysis between tracer intensity and pore density over length scales  
9 of the ROI (50  $\mu\text{m}$  x 150  $\mu\text{m}$ ).

10

## 11 Outflow Facility and Pore Density

12 Baseline outflow facilities were within the typical range for non-glaucomatous  
13 eyes (0.1 – 0.3  $\mu\text{L}/\text{min}/\text{mmHg}$ , see Table 1). Perfusion with tracer tended to  
14 decrease facility (Table 1), but tracer did not have a consistent or statistically  
15 significant effect across all eyes. Perfusion with gelatin did not significantly decrease  
16 outflow facility relative to the contralateral eye that was perfused without gelatin  
17 (Table 1).

18 The average total pore density observed across all six eyes was  $2173 \pm 471$   
19 pores/ $\text{mm}^2$  (mean  $\pm$  standard error of the mean). The average I-pore density was  
20  $866 \pm 153$  pores/ $\text{mm}^2$ , and the average B-pore density was  $1231 \pm 354$  pores/ $\text{mm}^2$   
21 (Table 2). Although B-pores constituted the overall majority of pores ( $53 \pm 6.2\%$  vs.  
22  $44 \pm 6.7\%$ , weighted mean), one pair of eyes (681/682) showed more I-pores than B-  
23 pores ( $62 \pm 7.2\%$  I-pores vs.  $36 \pm 5.1\%$  B-pores). The other two pairs had a  
24 majority of B-pores ( $35 \pm 4.9\%$  I-pores vs.  $62 \pm 3.7\%$  B-pores). The remainder of  
25 pores (typically 3-7%) were U-pores that could not be clearly classified, usually



1 because part of the pore was obscured from view preventing definitive identification  
2 of a cell border.

3

#### 4 **Relationship between Pore Density and Tracer Intensity**

5 An ANCOVA analysis applied to all 31 ROIs from 6 eyes showed a positive  
6 correlation between *TI* and total pore density ( $p = 0.044$ , Table 3). When ANCOVA  
7 was applied to each pore type separately, there was a statistically significant  
8 correlation between paracellular (B-pore) density and *TI* ( $p = 0.016$ ), but no  
9 relationship between transcellular (I-pore) density and *TI* ( $p = 0.54$ ; Table 3).

10 Because ANCOVA operates on raw pore density and *TI* values, and because  
11 there may be significant variability in the numerical values of these data between  
12 eyes, the outcome of the ANCOVA analysis may be biased by extreme values of  
13 pore density or *TI* that may exert high statistical leverage on the common slope of  
14 the ANCOVA regressions. Indeed, total pore density ( $p = 0.0003$ , ANOVA), B-pore  
15 density ( $p = 0.0008$ ) and *TI* ( $p = 0.0007$ ) were all significantly different between eyes.  
16 To account for this potential confounding factor, *TI* and pore density data were  
17 normalized as described in Methods, and normalized data from all eyes were  
18 aggregated together and analyzed using a single linear regression. Note that, as a  
19 result of the normalization, all data values are non-dimensional and are centered  
20 around 0 for *TI*\* and around 1 for normalized pore metrics (Figures 5 and 6).

21 There was a borderline significant correlation between the normalized pore  
22 density and *TI*\* when applied to total pores ( $p = 0.054$ ; Table 3), with a positive slope  
23 for the linear regression suggesting that pore density tends to increase with  
24 increasing *TI*\* across the entire population of ROIs (Figure 5). When analyzed in  
25 terms of pore subtypes, there was a slightly stronger statistical relationship for B-

1 pores ( $p = 0.051$ ) but not for I-pores ( $p = 0.27$ ; Table 3 and Figure 5), consistent with  
2 the ANCOVA results above. These results suggest that B-pores, more so than I-  
3 pores, tend to co-localize with regions of elevated tracer accumulation, presumably  
4 representing sites of greater fluid transport across the inner wall.

5

## 6 **Hydrodynamic models**

7 To understand how pore density ( $n$ ) and diameter ( $D$ ) may influence the local  
8 hydraulic conductivity ( $L_p$ ) of the outflow pathway, we examined the relationship  
9 between tracer intensity and  $L_p$  as predicted by the funneling model ( $L_p \sim nD$ ), the  
10 porosity model ( $L_p \sim nD^2$ ) and the Sampson's law model ( $L_p \sim nD^3$ ). Statistics were  
11 determined using both raw data analyzed by ANCOVA and normalized data  
12 analyzed by single linear regression. All regressions, regardless of the statistical  
13 approach, had a positive slope, and the correlations for the hydrodynamic models  
14 ( $nD$ ,  $nD^2$  and  $nD^3$ ) were all statistically stronger than those for the pore density alone  
15 (Table 3). By ANCOVA, a clear trend emerged:  $TI$  showed a highly significant  
16 positive correlation for all hydrodynamic models involving total pores ( $p < 0.0015$ )  
17 and B-pores ( $p < 0.000025$ ) but not for those involving I-pores ( $p > 0.38$ ; Table 3).  
18 The same trend was observed using normalized data, where all hydrodynamic  
19 models correlated strongly with  $TI^*$  for total pores ( $p < 0.027$ ) and B-pores ( $p <$   
20  $0.0037$ ) but not for I-pores ( $p > 0.10$ ; Table 3 and Figure 6). Presumably, the  
21 stronger correlations with B-pores overcame the weaker correlations with I-pores  
22 and contributed to the statistically significant correlations observed when both pore  
23 subtypes were aggregated and analyzed together as total pores.

24 To determine which hydrodynamic model gave the best fit to the tracer data,  
25 we compared the partial  $\eta^2$  values from the ANCOVA analysis and the  $R^2$  values

1 from the normalized analysis. For all hydrodynamic models the partial  $\eta^2$  and  $R^2$   
2 values were typically 45-fold and 5-fold greater for B-pores ( $\eta^2 > 0.53$ ,  $R^2 > 0.25$ )  
3 than I-pores ( $\eta^2 < 0.03$ ,  $R^2 < 0.09$ ), consistent with the stronger statistical  
4 relationships with B-pores presented above. The largest partial  $\eta^2$  value was  
5 observed for the B-pore porosity ( $nD^{2*}$ ) model ( $\eta^2 = 0.66$ ), while the largest  $R^2$  value  
6 was observed for the B-pore Sampson's law ( $nD^3$ ) model ( $R^2 = 0.32$ ; Table 3).  
7 However, the values of partial  $\eta^2$  and  $R^2$  were relatively similar between all three  
8 models, making it difficult to definitively determine which specific model best fit the  
9 data.

## 1 Discussion

2       Several studies have investigated how tracer particles pass through the  
3 trabecular outflow pathway, mostly by imaging transverse sections through the TM,  
4 JCT and SC endothelium (de Kater et al., 1989; Epstein and Rohen, 1991; Ethier  
5 and Chan, 2001; Lu et al., 2008; Overby et al., 2002). Some of these studies  
6 observed tracer particles close to pores (Chang et al., 2014; Ethier and Chan, 2001;  
7 Lu et al., 2008) or passing through pores (Allingham et al., 1992; Yang et al., 2013).  
8 However, the small number of pores typically observed in individual sections has  
9 prevented any detailed quantitative analysis of the relationship between tracer  
10 accumulation in the JCT and pores in the inner wall of SC. In the present work, this  
11 problem was overcome by sampling a large area of the inner wall using correlative  
12 microscopy to acquire co-registered images of inner wall pores (by SEM) and tracer  
13 distribution in the JCT (by confocal microscopy). Using this approach, a strong  
14 correlation was observed between tracer intensity and B-pore density and pore  
15 metrics, but no correlation was observed with I-pore density or pore metrics. These  
16 observations strongly argue that aqueous humor passes through micron-sized pores  
17 in the inner wall endothelium of SC, with a dominant hydrodynamic contribution from  
18 paracellular B-pores compared to transcellular I-pores. Furthermore, these  
19 observations demonstrate that the location of B-pores and the local hydraulic  
20 conductivity arising due to B-pores co-localizes with the non-uniform or segmental  
21 distribution of outflow through the JCT.

22       The fundamental assumption underlying this tracer study (and any tracer study)  
23 is that the tracer distribution reflects the pattern of aqueous humor outflow through  
24 the TM/JCT, such that regions of higher tracer accumulation correspond to regions  
25 of higher outflow. Indeed, prior tracer studies have shown that tracer accumulation

1 coincides with the location of collector channel ostia (Ethier et al., 1998; 1993; Hann  
2 and Fautsch, 2009; Zhang et al., 2009) and with regions of JCT containing less  
3 versican (M. C. Johnson et al., 1990; Keller et al., 2011), supporting this assumption.

#### 4 *Rationale for Immersion Fixation*

5       The current study used immersion fixation, although it is generally believed that  
6 perfusion fixation is necessary to preserve pores and giant vacuoles along the inner  
7 wall (Ethier et al., 2004; Overby, 2011). Pores and giant vacuoles, however, were  
8 commonly observed in the immersion-fixed samples of this study, suggesting that  
9 the two-step method of first immersing the eye in wet ice followed by immersion in  
10 ice cold fixative was able to preserve inner wall structure.

11       The motivation for the immersion fixation approach was three-fold. Firstly,  
12 perfusion fixation is believed to artificially increase inner wall pore density (Ethier et  
13 al., 1998; M. C. Johnson et al., 2002; Preibisch et al., 2009; Sit et al., 1997), and we  
14 wished to avoid this artifact so as to best examine the relationship between pore  
15 density and tracer intensity. Secondly, in the eyes perfused with gelatin, wet ice was  
16 necessary to ‘set’ the gelatin prior to aldehyde fixation. Thirdly, the rapid drop in  
17 temperature would quickly inhibit metabolic activity at the inner wall and decrease  
18 the fluidity of lipid membranes, which we presumed would inhibit pore closure and  
19 giant vacuole retraction and thereby preserve these structures until the inner wall  
20 was aldehyde fixed. Indeed, using estimates of the heat transfer rate through sclera,  
21 the temperature of the inner wall should decrease from 34°C to 4°C within 30  
22 seconds to 5 minutes<sup>2</sup> following immersion in ice cold water at 0°C. While t he eye is

---

<sup>2</sup> This is a heat transfer problem. We modelled the eye as a sphere of radius 12 mm with SC endothelium located 0.5 mm beneath the scleral surface (Goshtasby, 1988; Irshad et al., 2010), and assumed that the thermal conductivity of the sclera was 0.53 W/mK (Barton and Trembly, 2013; M. C. Johnson et al., 2002), that the specific heat capacity of the sclera was 4181 W/kg K, and that the surface of the sclera was

1 cooling, however, IOP decreases as fluid drains through the outflow pathway (recall  
2 that the perfusion tubes were clamped, preventing backflow through that route).  
3 Conservative estimates of the IOP decay indicate that it takes at least 20 minutes for  
4 IOP to decrease from 8 to 4 mmHg after clamping the perfusion tubing<sup>3</sup>. Even if the  
5 IOP was reduced immediately to 0 mmHg, pore closure would still likely require  
6 several minutes, based on best estimates of the giant vacuole retraction time  
7 (Brilakis and D. H. Johnson, 2001) and pore formation in other endothelia (Martinelli  
8 et al., 2013). Thus, the ‘cooling’ rate of the inner wall was likely faster than the  
9 turnover time for pore formation and closure, and this rapid cooling may have  
10 preserved the inner wall structure despite the absence of perfusion fixation.

11 We cannot eliminate the possibility that the rapid decrease in temperature  
12 somehow induced pore formation. Indeed, the pore densities observed in this study  
13 were consistent, but somewhat higher ( $2181 \pm 1336$  pores/mm<sup>2</sup>), than prior reports  
14 of inner wall pore density (835 – 1437 pores/mm<sup>2</sup>), even when prior values were  
15 corrected to account for the artificial increase in pore density caused by perfusion  
16 fixation (Allingham et al., 1992; M. C. Johnson et al., 2002). Alternatively, the  
17 temperature decrease may have differentially affected each pore type. Indeed,  
18 higher proportions of B-pores relative to I-pores were typically observed in this study,  
19 opposite to the ratio observed in other studies. Specifically, in this study 53% of all

---

either at a constant temperature (0°C; corresponding to the lower time limit) or at a constant heat flux with a heat transfer coefficient 44 W/m<sup>2</sup>K (corresponding to the upper time limit, neglecting natural convection) (Incropera and DeWitt, 2002; M. C. Johnson et al., 1992). Both boundary conditions have an analytical solution given by Schneider (Schneider, 1955) that, when using the parameter values given above, yield the time limits given in the main text.

<sup>3</sup> The eye was treated as an RC circuit with an outflow resistance of 5 mmHg min/μL and an ocular compliance of  $C = 1/(K_r P)$  with  $P = 6$  mmHg and  $K_r = 0.0215$  1/μL (McBain, 1958). The IOP therefore decreases according to  $P_o = e^{-t/RC}$ , where  $P_o$  is the initial pressure (8 mmHg), predicting that the eye reaches 4 mmHg at  $t = 20$  min. Note that the compliance increases as the pressure decreases, suggesting that this calculation slightly underestimates the actual time required for IOP to reach 4 mmHg.

1 observed pores were B-pores (Table 2), whereas in a prior study 30% of all  
2 observed pores were B-pores (Ethier et al., 1998). Importantly however, because the  
3 current study compared ROIs from within individual wedges, any temperature-  
4 induced pore formation needed to have affected each ROI differentially to influence  
5 our results, since any artifact that affected all ROIs uniformly would have been  
6 effectively eliminated by the statistical normalization. Furthermore, if temperature-  
7 induced pore formation were to account for the observed relationship between pore  
8 metrics and tracer intensity, it would have to occur preferentially in regions of higher  
9 tracer accumulation. While this possibility cannot be eliminated, it seems unlikely,  
10 and considering that perfusion fixation is already known to artificially increase pore  
11 density, immersion fixation on ice seems a reasonable alternative for preserving  
12 inner wall pore structure.

13

#### 14 *The Spatial Relationship Between Pores and Local Filtration*

15 The spatial correlation observed between pores and tracer suggests that pores  
16 are related to outflow segmentation, but does not provide insight as to the nature of  
17 such a relationship. There are two limiting scenarios for how pores may interact with  
18 flow. First, local filtration may trigger pore formation. In our prior work (Braakman et  
19 al., 2014), we established that cellular strain can induce pore formation in cultured  
20 SC cells, so it is possible that pore formation results from the cellular strain imposed  
21 by giant vacuole formation or inner wall ‘ballooning’ associated with transendothelial  
22 filtration as occurs in vivo. In this scenario, the inner wall functions as a “smart” filter,  
23 adjusting its porosity and local hydraulic conductivity to accommodate local  
24 variations in filtration demand arising from outflow segmentation, with biomechanical  
25 strain acting as the local signal for pore formation. The second scenario is that pore

1 formation may regulate local filtration. Because the hydraulic conductivity of a non-  
2 porous region of the inner wall is low due to tight junctions between SC cells, micron-  
3 sized pores are an apparent requirement for aqueous humor filtration across the  
4 inner wall (M. C. Johnson, 2006; M. C. Johnson et al., 1992). Local pore formation,  
5 possibly induced by paracrine or autocrine signals released by JCT, TM or SC cells,  
6 may thereby determine filtration patterns to influence outflow segmentation.

7       The current study is unable to determine which of these scenarios is most  
8 correct. However, we speculate that the physiological situation is a mix of both  
9 extremes, representing a coupled interaction between local filtration demands and  
10 the cellular biomechanics involved in giant vacuole and pore formation. For example,  
11 a recent study by Overby et al. (Overby et al., 2014) has shown that pore formation  
12 correlates with the stiffness of the subcortical cytoskeleton in SC cells and, in line  
13 with this observation, that glaucomatous SC cells eyes exhibit both a stiffer  
14 subcortical cytoskeleton and a reduced ability to form pores. This leads to an  
15 interesting question of whether variations in SC cell stiffness exist along the inner  
16 wall, and whether such variations in stiffness may coincide with variations in pore  
17 density. Regardless of the precise mechanism, the fact that pore density is reduced  
18 in glaucomatous eyes, and that impaired pore formation persists in glaucomatous  
19 SC cells in culture, suggests that disrupting the normal mechanism of SC pore  
20 formation leads to impaired filtration, contributing to outflow obstruction and IOP  
21 elevation in glaucoma.

22

### 23 *Differential Responses of I-pores and B-pores*

24       The relationships between pore metrics and tracer were much stronger for  
25 paracellular B-pores compared to transcellular I-pores, and the strong relationship



1 with B-pores likely contributed to the overall relationship that was observed between  
2 tracer and total pores. These results suggest that B-pores provide the dominant  
3 pathway for aqueous humor filtration across the inner wall. In contrast, I-pores  
4 showed no correlation with tracer intensity. While these data cannot exclude any  
5 potential role for I-pores, the data do suggest that I-pores function differently so as to  
6 be less conductive than B-pores at physiological pressure drops across the inner  
7 wall, as examined in this study. For example, the ultrastructure of the JCT or  
8 extracellular matrix underlying I-pores may be more resistive than that underlying B-  
9 pores. Alternatively, B-pores and I-pores may operate at different ranges of pressure  
10 drop across the inner wall or function under different time or length scales. For  
11 example, I-pores might require more time to become fully conductive or have smaller  
12 or larger hydrodynamic radii of influence than is captured by the 150 x 50  $\mu\text{m}$  size of  
13 the ROI. Regardless, the data strongly support a hydrodynamic role for B-pores, but  
14 we would caution against using these data to argue against any potential role of I-  
15 pores.

16       Like the two pore sub-types observed in SC, vascular and lymphatic endothelia  
17 also exhibit two pathways for transport, particularly for leukocyte diapedesis that may  
18 proceed via transcellular or paracellular routes. In endothelia that form well-  
19 developed intercellular junctions such as in the blood-brain barrier, leukocyte  
20 diapedesis occurs predominantly transcellularly, allowing the junctions to be  
21 maintained and barrier function to be preserved (Wedel-Parlow et al., 2011). In  
22 microvascular and lymphatic endothelia with less well-developed intercellular  
23 junctions, leukocyte diapedesis occurs predominantly paracellularly (Carman et al.,  
24 2007). Similarly, the pore type in SC endothelium may depend on the quality of the  
25 local junctions or paracrine or autocrine signals from TM, JCT and/or SC cells

1 potentially mediated by physical cues related to IOP or outflow (Alvarado et al.,  
2 2005).

3 In conclusion, this study demonstrated a colocalization between paracellular B-  
4 pores and local tracer accumulation along the inner wall of SC in human eyes  
5 perfused with fluorescent tracer nanospheres. These results strongly argue that  
6 pores provide a pathway for aqueous humor filtration across the inner wall and that  
7 the location of pores may contribute to the segmental distribution of aqueous humor  
8 outflow in the JCT. Increasing pore density is therefore a promising strategy to  
9 promote outflow and lower IOP in glaucoma.

10

1 **Figure Captions**

2 **Figure 1:** Aqueous humor outflow is non-uniform, or segmental, around the  
3 circumference of the trabecular meshwork (TM) over both macroscopic (order of a  
4 few mm) and microscopic length scales (order of a few tens of  $\mu\text{m}$ ). **A)** The internal  
5 face of a corneoscleral wedge of a human eye after removing the iris, ciliary body,  
6 retina and choroid. The TM is seen as a dense band of pigmented tissue located  
7 near the corneoscleral junction. **B)** A fluorescent micrograph of the internal surface  
8 of the TM in a human eye after perfusion with fluorescent tracer particles. The  
9 orientation is similar to the TM shown in panel A. Macroscopic segmental outflow  
10 variations are detected as variations in fluorescence intensity around the  
11 circumference of the TM containing active (arrowheads, stronger signal, more  
12 accumulated tracer) and less active (asterisks, weaker signal, less accumulated  
13 tracer) outflow regions. **C)** When looking at a microscopic section through the TM  
14 and SC (between blue lines), red and green tracer particles can be seen to pass  
15 through the TM and into SC (arrows) through the preferential pathway (within dashed  
16 lines Panels A-C are reproduced from Chang et al. 2014 (Chang et al., 2014) and  
17 permission will be requested from the publisher.

18

19 **Figure 2:** Schematic illustration of the hypothesis motivating this study. Outflow  
20 through the trabecular meshwork (TM) is non-uniform or segmental (curved blue  
21 arrows) such that some regions of the TM have high local outflow, and hence high  
22 local tracer accumulation, relative to regions with low outflow and low tracer  
23 accumulation. We hypothesize that regions of high local tracer intensity colocalize  
24 with regions of high local pore density along the inner wall of Schlemm's canal (SC).

25

1 **Figure 3:** A summary of the image registration algorithm used to map the confocal  
2 montage onto the overview scanning electron microscopic (SEM) montage so as to  
3 allow colocalization analysis between tracer intensity and inner wall pore density.  
4 Common landmarks (red dots) observed along the inner wall within the vimentin (top  
5 left) or CD31 montage (not shown) were manually selected and matched to the  
6 same physical landmarks in the SEM montage (middle left). A mapping algorithm  
7 then calculated the mathematical transformation that, when applied to the vimentin  
8 (or CD31) montage, allowed the corresponding landmarks to overlap those in the  
9 SEM montage (top right) with good precision (cf. Figure 4). The same mathematical  
10 transformation was then applied to the tracer montage (bottom left), providing a co-  
11 registered SEM-tracer overlay that was used for colocalization analysis between  
12 tracer intensity and pore density (bottom right). The white curves in the right panels  
13 represent the anterior and posterior boundaries of the inner wall, determined from  
14 the CD31 labeling (not shown).

15

16 **Figure 4:** Quality of the image registration algorithm based on a transformed CD31  
17 montage (green) overlaid onto the corresponding scanning electron microscopy  
18 (SEM) overview montage (grey) from eye 649C. The white boxes labeled 1-2 are  
19 shown at higher magnification in the lower panels. Green arrows indicate regions of  
20 good co-registration ( $< 2 \mu\text{m}$ ) while red arrows indicate regions of larger deviation  
21 (typically  $< 5 \mu\text{m}$ ). Macroscopic features of the inner wall are largely preserved and  
22 overlap between transformed CD31 and SEM images. Coincident structures are  
23 marked with an orange dotted curve for the CD31 image and a white dashed curve  
24 for the SEM image.

25

1 **Figure 5:** Normalized pore density ( $n^*$ ) plotted versus normalized tracer intensity  
2 ( $TI^*$ ) in the juxtacanalicular tissue (JCT) for total pores, transcellular I-pores and  
3 paracellular B-pores. Black lines through the data represent the optimal linear  
4 regressions of  $n^*$  vs  $TI^*$  with the purple dashed curves representing the 95%  
5 confidence bounds on each regression. The linear regressions were borderline  
6 significant for total pores ( $p = 0.054$ ) and B-pores ( $p = 0.051$ ), but not for I-pores ( $p =$   
7  $0.27$ ). Each point represents an individual region-of-interest ( $N = 31$ ) from the 6  
8 eyes. See methods for details of the normalization.

9

10 **Figure 6:** Normalized pore metrics from the hydrodynamic models plotted versus  
11 normalized tracer intensity ( $TI^*$ ) in the juxtacanalicular tissue (JCT) for total pores,  
12 transcellular I-pores and paracellular B-pores. Pore metrics represent the local  
13 hydraulic conductivity of the outflow pathway based on the funneling model ( $nD^*$ ),  
14 the porosity model ( $nD^{2*}$ ) and the Sampson's law model ( $nD^{3*}$ ) as described in  
15 Methods. Black lines through the data represent the optimal linear regressions, and  
16 the purple dashed curves represent the 95% confidence bounds on each regression.  
17 All linear regressions were statistically significant for total pores ( $p < 0.027$ ) and B-  
18 pores ( $p < 0.0037$ ), but not for I-pores ( $p > 0.10$ ; see Table 3). Each point represents  
19 an individual region-of-interest ( $N = 31$ ) from the 6 eyes. See methods for details of  
20 the normalization.

1 **Table captions**

2 **Table 1:** Donor and perfusion information. “Tracer” facility was the average facility  
3 measured during tracer perfusion. “Post-Tracer” facility was the average facility  
4 measured during the period after the anterior chamber was exchanged and perfused  
5 with DBG (with or without gelatin).

6

7 **Table 2:** Summary of the measured pore densities, the absolute number of pores  
8 and the percentage of I-pores and B-pores. Note that the total pore densities and  
9 percentages of I-pores and B-pores are provided as mean  $\pm$  standard error of the  
10 mean, whereas the total number of observed pores is a sum of all the observed  
11 pores.

12

13 **Table 3:** Summary of the correlations between tracer intensity and pore metrics.  
14 Bolded p-values highlighted in green indicate statistically significant correlations ( $p <$   
15  $0.05$ ); bold-italicized p-values highlighted in yellow indicate borderline significant  
16 correlations ( $0.10 < p < 0.05$ ); and p-values highlighted in red are not statistically  
17 significant ( $p > 0.10$ ).

- 1 Allingham, R.R., de Kater, A.W., Ethier, C.R., Anderson, P.J., Hertzmark, E.,  
2 Epstein, D.L., 1992. The relationship between pore density and outflow facility in  
3 human eyes. *Investigative Ophthalmology & Visual Science* 33, 1661–1669.
- 4 Alvarado, J.A., Yeh, R.-F., Franse-Carman, L., Marcellino, G., Brownstein, M.J.,  
5 2005. Interactions between endothelia of the trabecular meshwork and of  
6 Schlemm's canal: a new insight into the regulation of aqueous outflow in the eye.  
7 *Transactions of the American Ophthalmological Society* 103, 148.
- 8 Barton, M.D., Trembly, B.S., 2013. Experimental Eye Research. *Experimental Eye*  
9 *Research* 115, 216–223. doi:10.1016/j.exer.2013.07.029
- 10 Bill, A., Svedbergh, B., 1972. Scanning electron microscopic studies of the trabecular  
11 meshwork and the canal of Schlemm. *Acta Ophthalmol (Copenh)* 50, 295–320.
- 12 Braakman, S.T., Pedrigi, R.M., Read, A.T., Smith, J.A.E., Stamer, W.D., Ethier, C.R.,  
13 Overby, D.R., 2014. Experimental Eye Research. *Experimental Eye Research*  
14 127, 224–235. doi:10.1016/j.exer.2014.08.003
- 15 Brilakis, H.S., Johnson, D.H., 2001. Giant vacuole survival time and implications for  
16 aqueous humor outflow. *Journal of Glaucoma* 10, 277–283.
- 17 Carman, C.V., Sage, P.T., Sciuto, T.E., la Fuente, de, M.A., Geha, R.S., Ochs, H.D.,  
18 Dvorak, H.F., Dvorak, A.M., Springer, T.A., 2007. Transcellular Diapedesis Is  
19 Initiated by Invasive Podosomes. *Immunity* 26, 784–797.  
20 doi:10.1016/j.immuni.2007.04.015
- 21 Chang, J.Y.H., Folz, S.J., Laryea, S.N., Overby, D.R., 2014. Multi-Scale Analysis of  
22 Segmental Outflow Patterns in Human Trabecular Meshwork with Changing  
23 Intraocular Pressure. *Journal of Ocular Pharmacology and Therapeutics* 30,  
24 213–223. doi:10.1089/jop.2013.0182
- 25 Cohen, J., Cohen, P., West, S.G., Aiken, L.S., 2013. Applied multiple  
26 regression/correlation analysis for the behavioral sciences. Routledge.
- 27 de Kater, A.W., Melamed, S., Epstein, D.L., 1989. Patterns of aqueous humor  
28 outflow in glaucomatous and nonglaucomatous human eyes. A tracer study  
29 using cationized ferritin. *Archives of Ophthalmology* 107, 572.
- 30 Epstein, D.L., Rohen, J.W., 1991. Morphology of the trabecular meshwork and inner-  
31 wall endothelium after cationized ferritin perfusion in the monkey eye.  
32 *Investigative Ophthalmology & Visual Science* 32, 160–171.
- 33 Ethier, C.R., Ajersch, P., Pirog, R., 1993. An improved ocular perfusion system.  
34 *Current eye research* 12, 765–770.
- 35 Ethier, C.R., Chan, D.W.H., 2001. Cationic ferritin changes outflow facility in human  
36 eyes whereas anionic ferritin does not. *Investigative Ophthalmology & Visual*  
37 *Science* 42, 1795–1802.
- 38 Ethier, C.R., Coloma, F.M., 1999. Effects of ethacrynic acid on Schlemm's canal  
39 inner wall and outflow facility in human eyes. *Investigative Ophthalmology &*  
40 *Visual Science* 40, 1599–1607.
- 41 Ethier, C.R., Coloma, F.M., Sit, A.J., Johnson, M.C., 1998. Two pore types in the  
42 inner-wall endothelium of Schlemm's canal. *Investigative Ophthalmology &*  
43 *Visual Science* 39, 2041–2048.
- 44 Ethier, C.R., Read, A.T., Chan, D.W.H., 2004. Biomechanics of Schlemm's Canal  
45 Endothelial Cells: Influence on F-Actin Architecture. *Biophysical Journal* 87,  
46 2828–2837. doi:10.1529/biophysj.103.038133
- 47 Ethier, C.R., Read, A.T., Chan, D.W.H., 2006. Effects of Latrunculin-B on Outflow  
48 Facility and Trabecular Meshwork Structure in Human Eyes. *Investigative*  
49 *Ophthalmology & Visual Science* 47, 1991–1998. doi:10.1167/iovs.05-0327
- 50 Goshtasby, A., 1988. Image registration by local approximation methods. *Image and*

- 1 Vision Computing 6, 255–261.
- 2 Grant, W.M., 1963. Experimental aqueous perfusion in enucleated human eyes.  
3 Archives of Ophthalmology 69, 783.
- 4 Hann, C.R., Fautsch, M.P., 2009. Preferential fluid flow in the human trabecular  
5 meshwork near collector channels. Investigative Ophthalmology & Visual  
6 Science 50, 1692–1697. doi:10.1167/iovs.08
- 7 Happel, J., Brenner, H., 1983. Low Reynolds number hydrodynamics: with special  
8 applications to particulate media. Springer.
- 9 Incropera, F.P., DeWitt, D.P., 2002. External Flow around a Sphere. Heat and Mass  
10 Transfer, Fifth Edition, John Wiley and Sons, NJ 533–593.
- 11 Irshad, F.A., Mayfield, M.S., Zurakowski, D., Ayyala, R.S., 2010. Variation in  
12 Schlemm's Canal Diameter and Location by Ultrasound Biomicroscopy.  
13 Ophthalmology 117, 916–920. doi:10.1016/j.ophtha.2009.09.041
- 14 Johnson, M.C., 2006. "What controls aqueous humour outflow resistance?"  
15 Experimental Eye Research 82, 545–557. doi:10.1016/j.exer.2005.10.011
- 16 Johnson, M.C., Chan, D.W.H., Read, A.T., Christensen, C., Sit, A.J., Ethier, C.R.,  
17 2002. Glaucomatous eyes have a reduced pore density in the inner wall  
18 endothelium of Schlemm's canal. Investigative Ophthalmology and Visual Science  
19 43, 3961.
- 20 Johnson, M.C., Johnson, D.H., Kamm, R.D., DeKater, A.W., Epstein, D.L., 1990.  
21 The filtration characteristics of the aqueous outflow system. Experimental Eye  
22 Research 50, 407–418.
- 23 Johnson, M.C., Shapiro, A., Ethier, C.R., Kamm, R.D., 1992. Modulation of outflow  
24 resistance by the pores of the inner wall endothelium. Investigative  
25 Ophthalmology & Visual Science 33, 1670–1675.
- 26 Keller, K.E., Bradley, J.M., Vranka, J.A., Acott, T.S., 2011. Segmental Versican  
27 Expression in the Trabecular Meshwork and Involvement in Outflow Facility.  
28 Investigative Ophthalmology & Visual Science 52, 5049–5057.  
29 doi:10.1167/iovs.10-6948
- 30 Lu, Z., Overby, D.R., Scott, P.A., Freddo, T.F., Gong, H., 2008. The mechanism of  
31 increasing outflow facility by rho-kinase inhibition with Y-27632 in bovine eyes.  
32 Experimental Eye Research 86, 271–281. doi:10.1016/j.exer.2007.10.018
- 33 Lütjen-Drecoll, E., 1973. Structural Factors Influencing Outflow Facility and its  
34 Changeability Under Drugs A Study in Macaca Arctoides. Investigative  
35 Ophthalmology & Visual Science 12, 280–294.
- 36 Martinelli, R., Kamei, M., Sage, P.T., Massol, R., Varghese, L., Sciuto, T., Toporsian,  
37 M., Dvorak, A.M., Kirchhausen, T., Springer, T.A., Carman, C.V., 2013. Release  
38 of cellular tension signals self-restorative ventral lamellipodia to heal barrier  
39 micro-wounds. The Journal of Cell Biology 201, 449–465. doi:10.1182/blood-  
40 2004-12-4942
- 41 Mäepea, O., Bill, A., 1992. Pressures in the juxtacanalicular tissue and Schlemm's  
42 canal in monkeys. Experimental Eye Research 54, 879–883.
- 43 McBain, E.H., 1958. Tonometer Calibration. AMA Arch Ophthalmol 60, 1080.  
44 doi:10.1001/archophth.1958.00940081100015
- 45 Overby, D.R., 2011. The mechanobiology of aqueous humor transport across  
46 Schlemm's canal endothelium. Mechanobiology Handbook 367–390.
- 47 Overby, D.R., Gong, H., Qiu, G., Freddo, T.F., Johnson, M.C., 2002. The mechanism  
48 of increasing outflow facility during washout in the bovine eye. Investigative  
49 Ophthalmology & Visual Science 43, 3455–3464.
- 50 Overby, D.R., Zhou, E.H., Vargas-Pinto, R., Pedrigi, R.M., Fuchshofer, R.,



- 1 Braakman, S.T., Gupta, R., Perkumas, K.M., Sherwood, J.M., Vahabikashi, A.,  
2 Dang, Q., Kim, J.H., Ethier, C.R., Stamer, W.D., Fredberg, J.J., Johnson, M.C.,  
3 2014. Altered mechanobiology of Schlemm's canal endothelial cells in glaucoma.  
4 Proceedings of the national Academy of Sciences.  
5 doi:10.1073/pnas.1410602111
- 6 Preibisch, S., Saalfeld, S., Tomancak, P., 2009. Globally optimal stitching of tiled 3D  
7 microscopic image acquisitions. *Bioinformatics* 25, 1463–1465.  
8 doi:10.1093/bioinformatics/btp184
- 9 Schneider, P.J., 1955. *Conduction Heat Transfer*. Addison-Wesley Publishing  
10 Company.
- 11 Sit, A.J., Coloma, F.M., Ethier, C.R., Johnson, M.C., 1997. Factors affecting the  
12 pores of the inner wall endothelium of Schlemm's canal. *Investigative*  
13 *Ophthalmology & Visual Science* 38, 1517–1525.
- 14 Wedel-Parlow, von, M., Schrot, S., Lemmen, J., Treeratanapiboon, L., Wegener, J.,  
15 Galla, H.-J., 2011. Neutrophils cross the BBB primarily on transcellular pathways:  
16 An in vitro study. *Brain Research* 1367, 62–76.  
17 doi:10.1016/j.brainres.2010.09.076
- 18 Yang, C.Y.C., Liu, Y., Lu, Z., Ren, R., Gong, H., 2013. Effects of Y27632 on  
19 Aqueous Humor Outflow Facility With Changes in Hydrodynamic Pattern and  
20 Morphology in Human Eyes. *Multiple values selected* 54, 5859–5870.  
21 doi:10.1167/iovs.12-10930
- 22 Zhang, Y., Toris, C.B., Liu, Y., Ye, W., Gong, H., 2009. Morphological and  
23 hydrodynamic correlates in monkey eyes with laser induced glaucoma.  
24 *Experimental Eye Research* 89, 748–756. doi:10.1016/j.exer.2009.06.015  
25

Figure 1  
[Click here to download Figure\(s\): Figure 1.pdf](#)

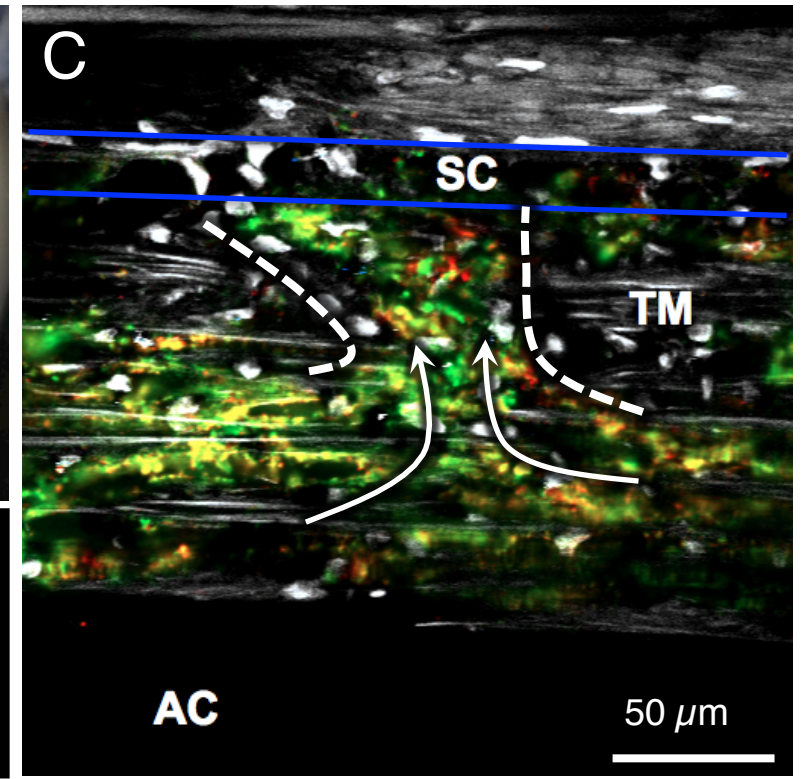
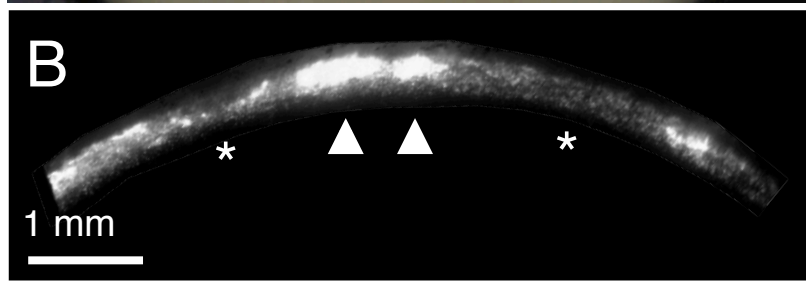
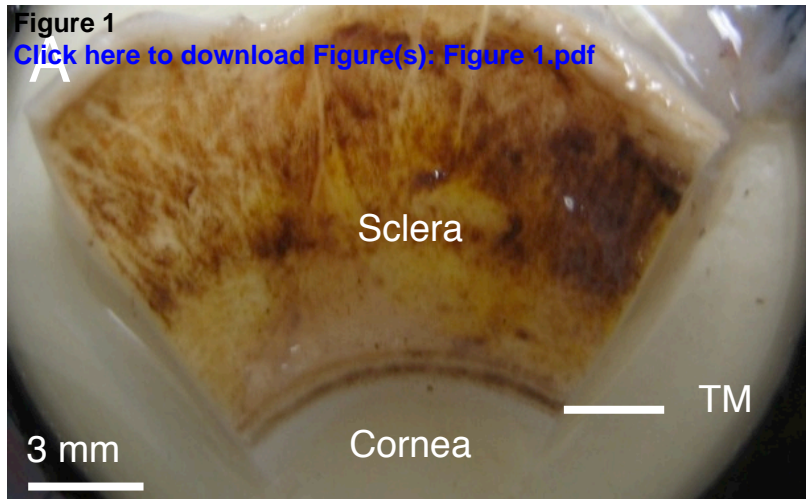


Figure 2

[Click here to download Figure\(s\): Figure 2.pdf](#)

TM

Inner Wall

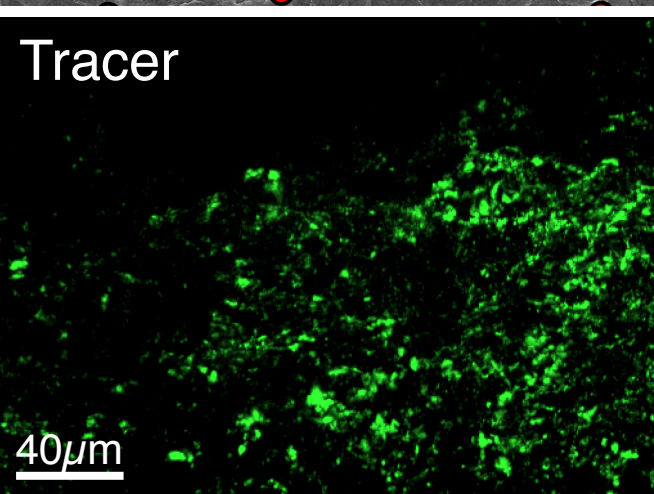
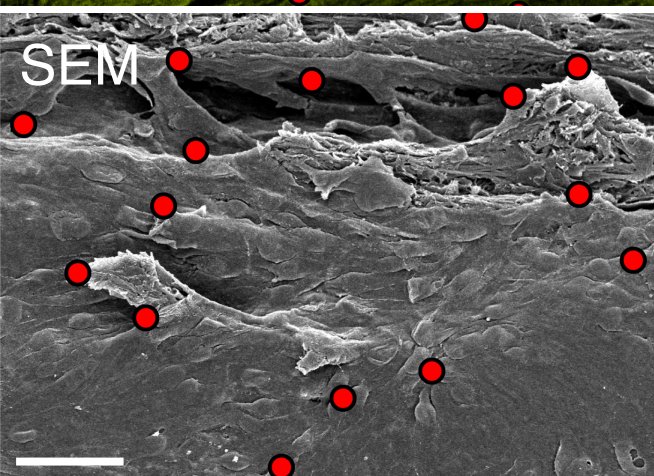
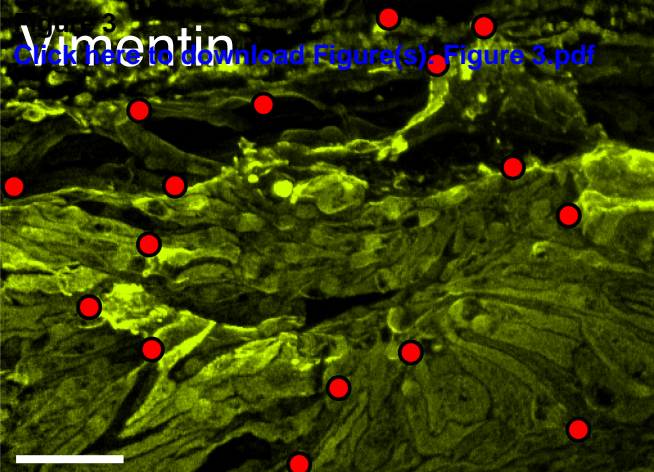
SC Lumen



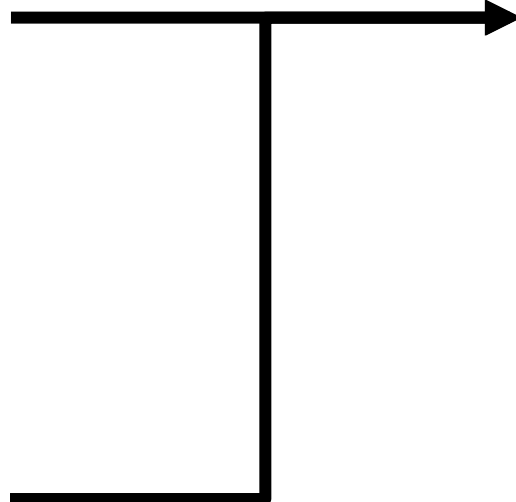
*Low Tracer  
Few Pores?*

*High Tracer  
Many Pores?*

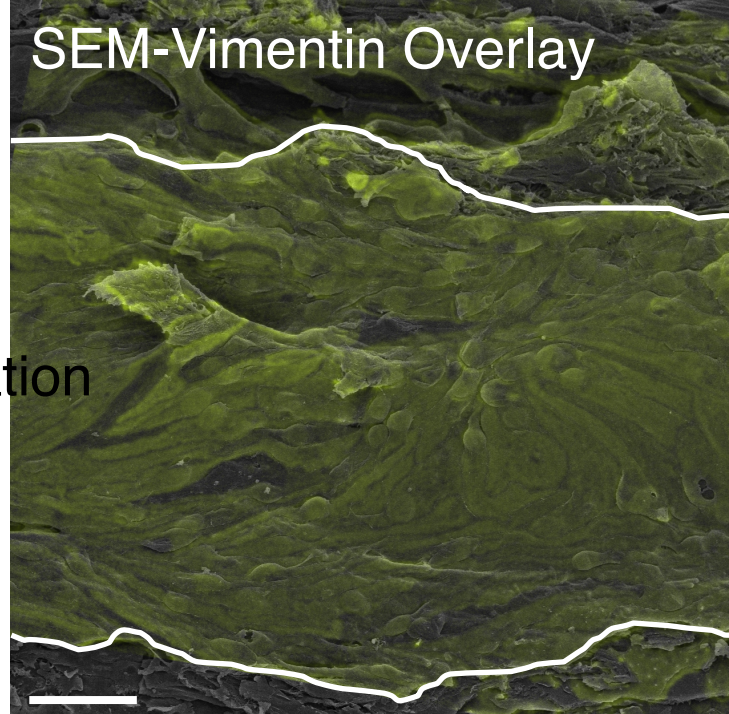




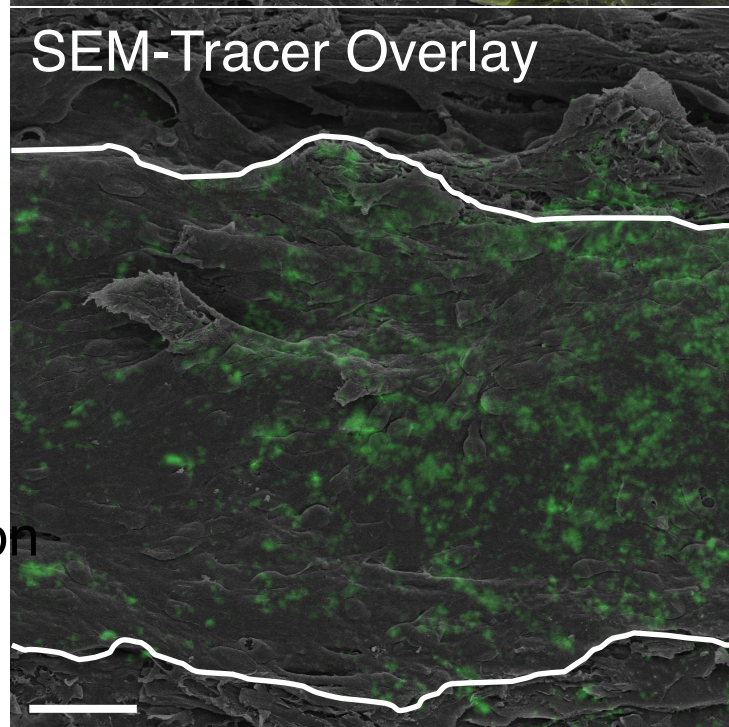
Calculate Transformation



SEM-Vimentin Overlay



SEM-Tracer Overlay



Apply Transformation



Figure 4

[Click here to download Figure\(s\): Figure 4.pdf](#)

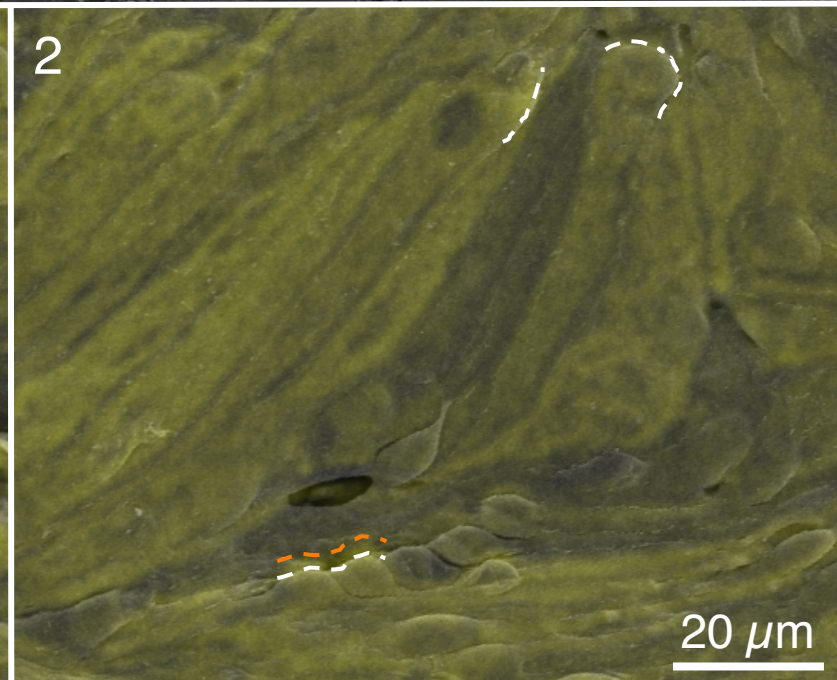
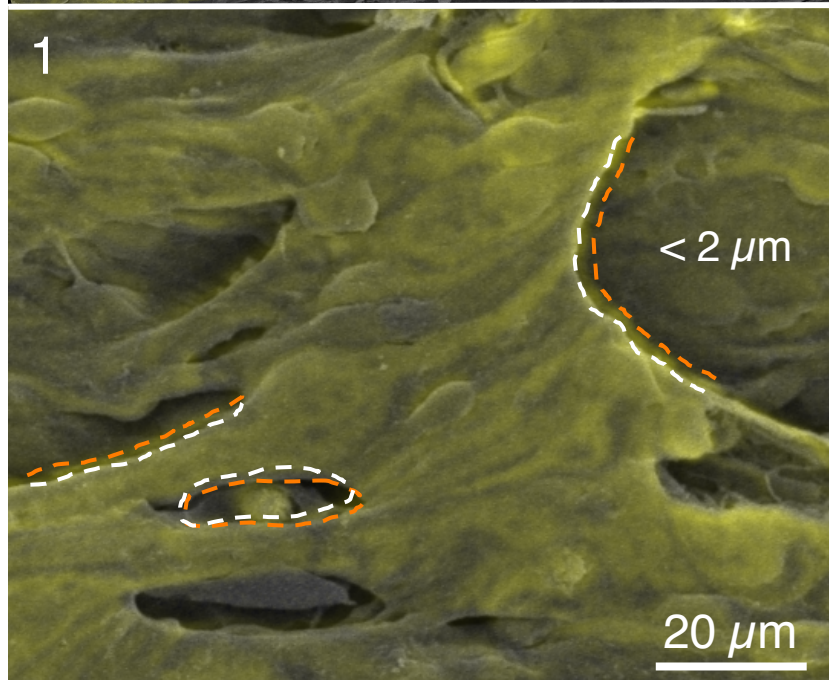
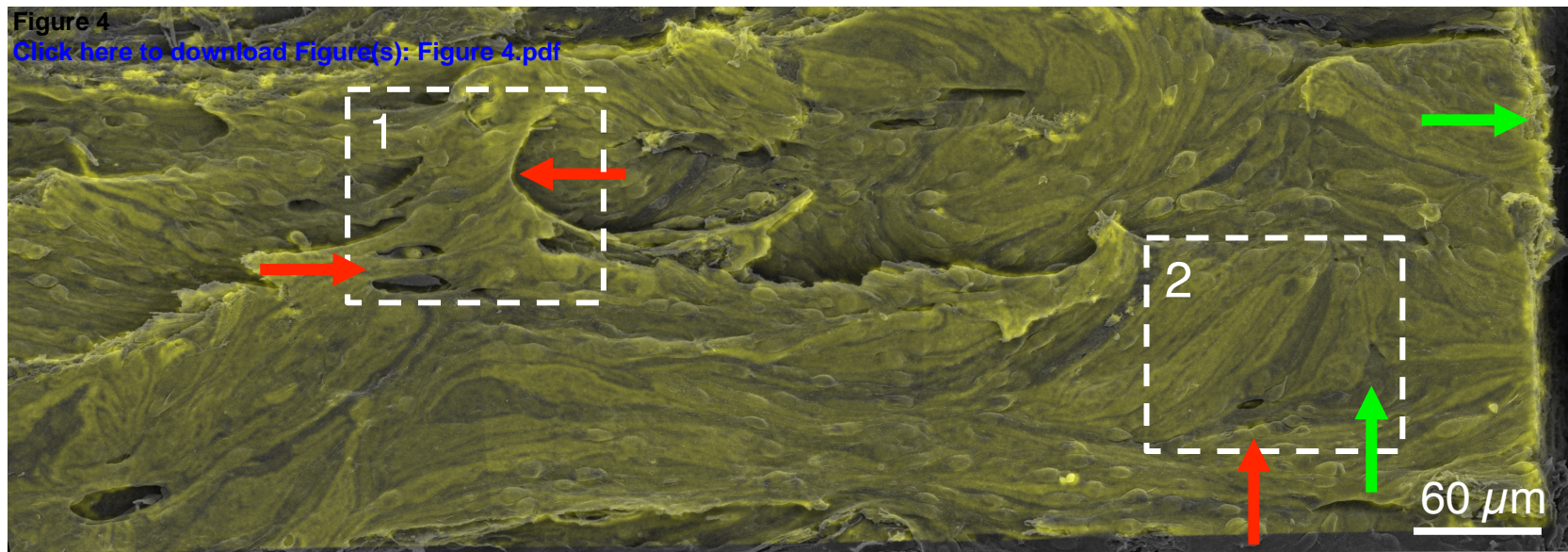


Figure 5 Total pores

[Click here to download Figure\(s\): Figure 5.pdf](#)

I-pores

B-pores

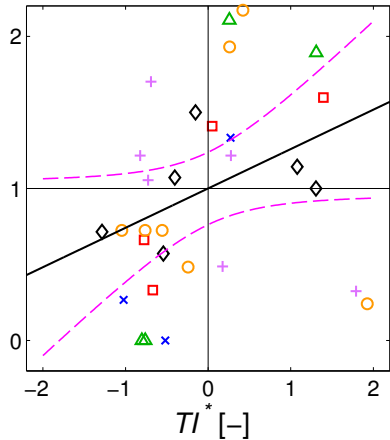
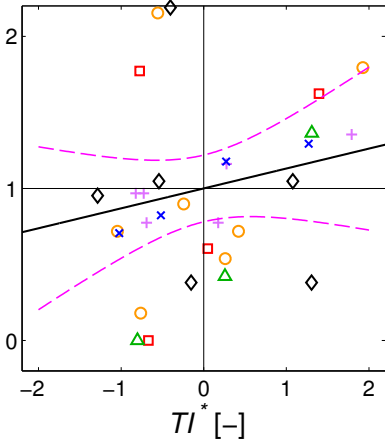
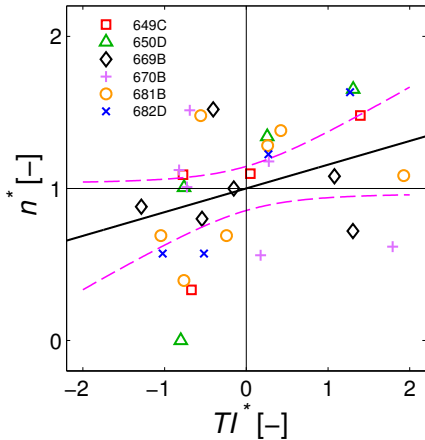
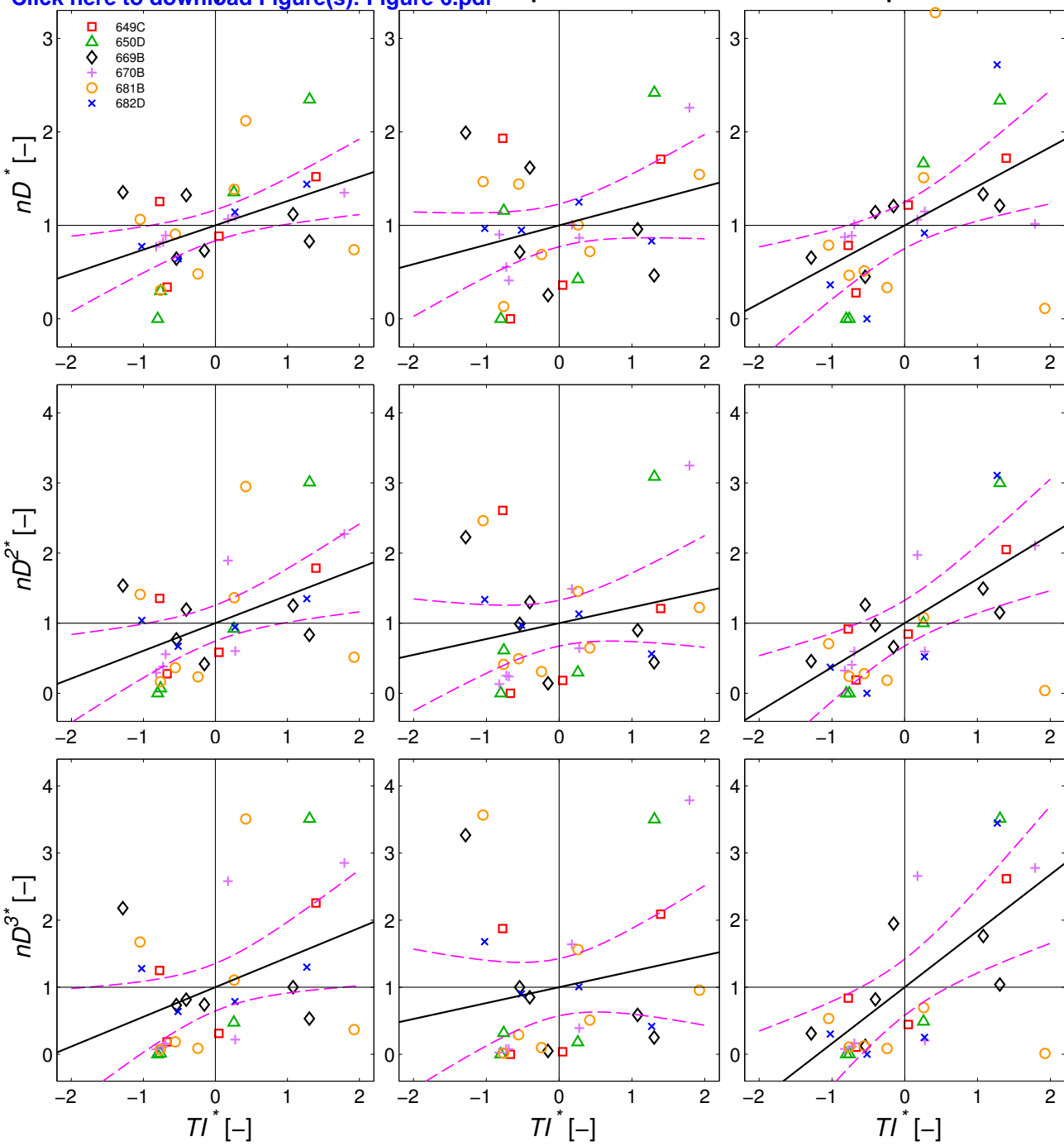


Figure 6

Total pores

I-pores

B-pores

[Click here to download Figure\(s\): Figure 6.pdf](#)

**Table 1**[Click here to download Table\(s\): Table 1.xlsx](#)

Number	Eye		Sex	Age	Time [hrs Post Mortem]		Facility [ $\mu$ L/min/mmHg]			Gelatin Present
	L/R	Comments			Enucleation	Perfusion	Baseline	Tracer	Post-Tracer	
649	L	None	M	67	5	34	0.30	0.20	0.17	No
650	R	Aphakic					0.16	0.10	0.10	Yes
669	L	None	F	80	1	22	0.10	0.15	0.09	No
670	R	None					0.12	0.20	0.16	Yes
681	R	Pseudophakic	M	78	6	28	0.30	0.25	0.17	No
682	L	Pseudophakic					0.19	0.18	0.18	Yes



Table 2

[Click here to download Table\(s\): Table 2.xlsx](#)

Eye	Average pore density [ $1/\text{mm}^2$ ]			Number of observed pores			Percentage of Total	
	Total pores	I-pores	B-pores	Total pores	I-pores	B-pores	% I-pores	% B-pores
649C	3635	911	2440	105	26	71	25%	<b>68%</b>
650D	704	320	384	20	9	11	45%	<b>55%</b>
669B	3333	1400	1867	150	63	84	42%	<b>56%</b>
670B	2378	689	1644	107	31	74	29%	<b>69%</b>
681B	1352	743	552	71	39	29	<b>55%</b>	41%
682D	1633	1133	500	49	34	15	<b>69%</b>	31%
<b>Total</b>	<b>2173±471</b>	<b>866±153</b>	<b>1231±354</b>	<b>382</b>	<b>129</b>	<b>240</b>	44±6.7%	<b>53±6.2%</b>

Table 3

[Click here to download Table\(s\): Table 3.xlsx](#)

Model		Total pores			I-pores			B-pores		
ANCOVA Raw Data		p	Partial $\eta^2$	Slope	p	Partial $\eta^2$	Slope	p	Partial $\eta^2$	Slope
	n	<b>0.044</b>	0.16	+	0.54	0.02	+	<b>0.016</b>	0.22	+
	nD	<b>1.5E-03</b>	0.35	+	0.38	0.03	+	<b>2.5E-05</b>	0.53	+
	nD <sup>2</sup>	<b>3.2E-04</b>	0.42	+	0.84	0.00	+	<b>4.8E-07</b>	0.66	+
	nD <sup>3</sup>	<b>4.0E-04</b>	0.41	+	0.81	0.00	+	<b>1.9E-06</b>	0.62	+
t-test Normalized Data		p	R <sup>2</sup>	Slope	p	R <sup>2</sup>	Slope	p	R <sup>2</sup>	Slope
	n <sup>*</sup>	<b>0.054</b>	0.12	+	0.27	0.04	+	<b>0.051</b>	0.12	+
	nD <sup>*</sup>	<b>0.006</b>	0.22	+	0.10	0.09	+	<b>3.7E-03</b>	0.25	+
	nD <sup>2*</sup>	<b>0.007</b>	0.22	+	0.21	0.05	+	<b>1.1E-03</b>	0.30	+
	nD <sup>3*</sup>	<b>0.027</b>	0.15	+	0.31	0.03	+	<b>7.8E-04</b>	0.32	+